Journal of Power Sources 564 (2023) 232814

Contents lists available at ScienceDirect

Journal of Power Sources

journal homepage: www.elsevier.com/locate/jpowsour

Numerical analysis of vanadium redox flow batteries considering electrode deformation under various flow fields

Binyu Xiong [a], Yang Li [b,**], Yuming Ding [a], Jinsong Wang [c], Zhongbao Wei [d], Jiyun Zhao [e], Xiaomeng Ai [f], Jiakun Fang [f,*]

[a] School of Automation, Wuhan University of Technology, Wuhan, 430070, China
[b] Department of Electrical Engineering, Chalmers University of Technology, Sweden
[c] Case School of Engineering, Case Western Reserve University, Cleveland, OH, 44106, USA
[d] Beijing Institute of Technology, National Engineering Laboratory for Electric Vehicles, 100081, Beijing, China
[e] Department of Mechanical Engineering, City University of Hong Kong, 83 Tat Chee Avenue, Kowloon, Hong Kong
[f] State Key Laboratory of Advanced Electromagnetic Engineering and Technology, School of Electrical and Electronic Engineering, Huazhong University of Science and Technology, Wuhan, 430074, China

HIGHLIGHTS

- A 3D electrochemical model considering unevenly electrodes deformation is proposed.
- A non-uniform partitioning method for unevenly deformed electrodes is proposed.
- The compression ratios under various mechanical stress are measured.
- The interdigitated flow channels under CR of 45% demonstrate maximum performance.

ARTICLE INFO

Keywords:
Vanadium redox flow battery
Uneven electrode deformation
Flow channel
Electrochemical model
Battery design
Numerical study

ABSTRACT

The porous electrode of vanadium redox flow batteries (VRBs) is subject to deformation due to mechanical stress during stack assembling. The forces compress the electrode fiber into the flow channel and thus alter the electrode porosity ratio. Due to the complex mechanisms, the effects of resulting electrode morphological changes on VRB performance were usually ignored in existing studies. This paper proposes a three-dimensional VRB model considering the uneven electrode deformation to investigate the cell performance under different electrode compression ratios with three flow-field designs. Compression ratio (CR) and the intrusive part of the electrode are obtained under various mechanical stress by adjusting gasket thickness in the experiment. The proposed electrochemical model is established based on the comprehensive description of conservation laws and analyzed using the COMSOL platform. Three indices, namely the concentration overpotential, pressure drop, and distribution uniformity, are selected for the analysis under the three flow field designs and different CRs. The numerical study reveal that the pressure drop and the concentration overpotential are sensitive to the CR but less affected by the concentration uniformity. The minimum overpotential can be reached when the CR is around 40%–50%, depending on flow field designs, while a higher CR can cause a drastically increased pressure drop. It is also found that the interdigitated flow field with a CR of 45% is considered optimal. The insights from the proposed method demonstrate the significance of considering the effects of electrode deformation in the stack design under various flow fields.

1. Introduction

The vanadium redox flow battery (VRB) has been widely implemented for large-scale stationary energy storge due to its safe operation, design flexibility, long life span, and high system efficiency [1]. With the rapid development of VRBs, the improvement of stack

* Corresponding author.
** Corresponding author.
E-mail addresses: bxiong2@whut.edu.cn (B. Xiong), yangli@ieee.org (Y. Li), jiyuzhao@cityu.edu.hk (J. Zhao), jfa@hust.edu.cn (J. Fang).

https://doi.org/10.1016/j.jpowsour.2023.232814
Received 5 August 2022; Received in revised form 27 December 2022; Accepted 11 February 2023
Available online 1 March 2023

performance has become a crucial task for commercialization [2]. Extensive efforts have been made to enhance stack performance [3]. Methods including new material fabrications [4,5], optimal stack designs [6,7], and operational control strategies [8,9] are proposed to improve the stack performance at different life-cycle stages of VRBs. Notably, since the flow pattern can significantly affect the electrolyte concentration distribution, overpotential, and overall pressure drop, research has been directed to the flow channel design at the stack assembling stage [10,11].

In previous studies, various designs of flow channels were proposed to enhance VRB performance. The typical channel designs are the parallel flow channels [12], serpentine flow channels [13], and interdigitated flow channels [14]. Chen et al. [15] simulated a cell with parallel flow channels using the computational fluid dynamics (CFD) method and validated the model through cell performance experiments. Jiao et al. [16] investigated cells containing serpentine flow channels. Lu et al. [17] conducted numerical analysis on VRB cells compared with serpentine flow channel and interdigitated flow channel. Messaggi et al. [18] constructed a 3D computational fluid dynamics model of the VRB cells to simulate the effects of a single serpentine flow channel and an interdigitated flow channel. The studies indicated that the flow channel could affect the hydraulic pressure drop and influence the electrolyte uniformity of the porous electrodes for chemical reactions.

A few studies have focused on the effects of electrode morphological changes due to the clamping force. During the stack assembling process, multiple cells are squeezed and compressed in series [19]. Due to mechanical stress, the porous electrodes will be deformed, and part of the fibers will be intruded into the flow channels. This morphological deformation varies the porosity of the electrodes, leading to uneven distribution in different regions. Specifically, the porous electrode region beneath the flow field ribs bears a great deal of mechanical stress and thus is deformed to be less porous. The rest part of the electrode would compressed into the electrolyte flow channel since there is less mechanical stress. This uneven porosity distribution could affect the electrolyte transport and cell performance. The compression ratio (CR) is a critical indicator of the degree of electrode compression or deformation. A high CR can lead to a reduction of contact resistance and a high voltage efficiency, whereas it may also result in high pressure drops and extra parasitic losses. Thus, the electrode deformation needs to be considered when assessing the overall performance of VRB. Several studies have been conducted to evaluate the effects of electrode deformation on stack performance through experiments and simulations. Park et al. [20] conducted experiments to investigate the influence of compressed carbon felt electrodes on the performance of VRB. The energy efficiency of the cell may increase with the increase of CR, and the maximum efficiency is reached when the CR is around 20%. However, the experiment is time-consuming, and the experimental materials are expensive. Another cost-effective approach to facilitate stack design is to set up an electrochemical model and analyze the overall performance. This method is feasible to estimate the internal mass transfer process of the electrolyte via numerical analysis. You et al. [21] firstly set up a two-dimensional steady-state model to describe VRBs, focusing on the effect of electrode porosity on cell performance. It was exhibited that a decrease in electrode porosity could lead to a faster depletion of reactant concentration, resulting in a more uniform overpotential distribution. Later, Bromberger et al. [22] developed a model of a two-dimensional VRB to investigate the effect of electrode compression on voltage loss and hydrodynamics. The authors show that a certain degree of electrode compression could reduce the area-specific resistance, porosity, and hydraulic permeability. The optimal CR depends on the material properties and porosity. Then, three-dimensional models were established to explain the complex fluid dynamics and mass transfer processes in porous electrodes. Oh et al. [23] developed a three-dimensional model to investigate the VRB's performance with electrode CRs of 10% and 20%. The effect of electrode compression was evaluated by analyzing the potential distribution, transfer current density, vanadium concentration distribution, and overall charge and discharge performance. Brown et al. [24] extended the electrode CRs ranging from 0% to 75% to analyze the electrode compression effects on cell performance, which indicated that a high CR of the electrodes could reduce ohmic losses and increase energy efficiency. However, the compression stress of the electrode is not evenly distributed. The deformation under the rib region is more significant than that under the flow channel. Wang et al. [25] proposed a non-uniform model of VRB to describe this unique phenomenon and investigated the performance of the cell with serpentine flow channels under different local CRs. Moreover, the uneven deformation of the electrodes under various flow rates was not fully revealed yet.

The main contributions of this paper are summarized as.

(1) An electrochemical model considering the unevenly deformed electrodes is proposed to analyze the impact on mechanical stress in practical applications.
(2) A novel partitioning method for unevenly deformed electrodes is introduced, and the compression ratios under various mechanical stress are measured.
(3) An insight into the electrode deformation and the flow fields optimization are suggested to improve the overall performance in terms of overpotential, pressure drop, and uniformity of concentration distribution.

This paper is organized as follows. The development of the 3D electrochemical model considering electrode deformation is described in Section 2. The experimental validation for the 3D electrochemical model is performed in Section 3, and then the three indices are analyzed to further demonstrate the cell performance under various compression ratios. The conclusions are summerized in Section 4.

2. Electrochemical model development

An electrochemical model is needed to describe the inner multiphysics behavior of the stacks. A typical VRB cell consists of bipolar plates engraved with membranes, flow channels, bipolar plates, porous electrodes, tanks, pumps, and current collectors. The charging and discharging chemical reactions are shown as follows:

Positive electrode:

$$VO^{2+} + H_2O - e^- \rightleftharpoons VO_2^+ + 2H^+ \tag{1}$$

Negative electrode:

$$V^{3+} + e^- \rightleftharpoons V^{2+} \tag{2}$$

The following hypotheses are made to simplify the model setup and reduce the simulation time:

1) A laminar flow is assumed for the electrolyte, and the electrolyte is incompressible.
2) The properties of the cell materials are isotropic and homogeneous.
3) There are no side reactions and electrolyte leakage.
4) The electrolyte is a dilute solution in the simulation.
5) Since the electrochemical time constant is smaller than the time required for significant variations in the ion concentration in the electrolyte, the process is considered isothermal and static.

To describe the remaining capacity of the cell, state of charge (*SOC*) is defined as:

$$SOC = \frac{c_2}{c_0} \times 100\% = \frac{c_5}{c_0} \times 100\% \tag{3}$$

where c_2 is the molar concentration of V^{2+} in the negative electrode, c_5 is the molar concentration of VO_2^+ in the positive electrode, and c_0 is the initial concentration of vanadium ions.

2.1. Geometric details and compression ratios

An electrochemical model with different compression ratios needs to be developed to describe the electrode deformation under various mechanical stresses. An illustration of a VRB cell with unevenly compressed electrodes is shown in Fig. 1. The geometric details of deformed carbon felt are shown in Fig. 1 (a). Due to the mechanical stress, the electrodes can be unevenly compressed the physical electrode into two regions, including the intrusion electrode region and the rib region as shown in Fig. 1(b). The intrusion electrode region is subject to less mechanical stress beneath the flow channel. On the contrary, the rib region is subject to much mechanical stress. In this paper, a surface area with the width (W) of 30 mm and the length (L) of 30 mm are designed for the experiments.

The electrode parameters are related to the degree of electrode deformation. To describe to what extent the electrode is compressed, the electrode compression ratio (CR) is defined as:

$$CR = \left(1 - \frac{h_e}{h_0}\right) \times 100\% \tag{4}$$

where h_0 is the initial electrode thickness (initial height of 6 mm), and h_e is the porous electrode thickness.

Three flow channels are selected for numerical analysis to fully investigate the effect of different flow channels on battery performance. The three flow channel designs, including the parallel, serpentine, and interdigitated flow channels, are shown in Fig. 2.

2.2. Governing equations

The electrochemical model is established as coupled partial differential equations based on mass conservation, momentum conservation, charge conservation, and reaction kinetics [23,26].

For momentum conservation, the Brinkmann equation is applied to describe the porous medium flow in the electrode and the laminar flow in the flow channel. This mass balance is established with the incompressibility assumption:

$$\nabla \cdot \vec{u} = 0 \tag{5}$$

$$\frac{\mu}{K}\vec{u} = -P + \mu^*\left[\nabla\vec{u} + (\nabla\vec{u})^T\right] \tag{6}$$

where $\vec{\mu}$ represents the velocity, μ and μ^* represent the inherent and effective viscosity of the electrolyte, respectively, and P represents the pressure. Mass continuity and momentum continuity are automatically established at the flow channel and electrode contact surfaces. K is the permeability of the electrode and is described by the Carman-Kozeny equation [27]:

$$K = \frac{d_f^2 \varepsilon^3}{16 k_{CK}(1-\varepsilon^2)} \tag{7}$$

where ε represents the electrode porosity, d_f represents the fiber diameter, and C represents the Carman-Kozeny constant with a value of 5.55.

The concentration flux $\vec{N_i}$, is expressed through the modified Nernst-Planck equation [28], where the molar fluxes of species are considered a combination of diffusion, electromigration, and convection.

$$\vec{N_i} = -D_i^{eff}\nabla c_i - \frac{F z_i D_i^{eff}}{RT}\nabla\varphi + \vec{u}c_i \tag{8}$$

where φ denotes the overpotential, $\vec{N_i}$ denotes the concentration fluxes, c_i represents the concentration of the species i, $i \in \{V^{2+}, V^{3+}, VO^{2+}, VO_2^+, H^+, SO_4^{-2}\}$, z_i is the valence for species i, and D_i^{eff} is the effective diffusion coefficient.

According to the principle of electrical neutrality, the concentration of one of the species is determined according to the other species:

$$\sum_i z_i c_i = 0 \tag{9}$$

The effective diffusion coefficient under the correction of Bruggeman is [29]:

$$D_i^{eff} = \varepsilon^{3/2} D_i \tag{10}$$

For the reactions on porous electrode surfaces, the Butler-Volmer law can be applied to describe the reversible redox properties. The transfer current densities on the negative and the positive sides are:

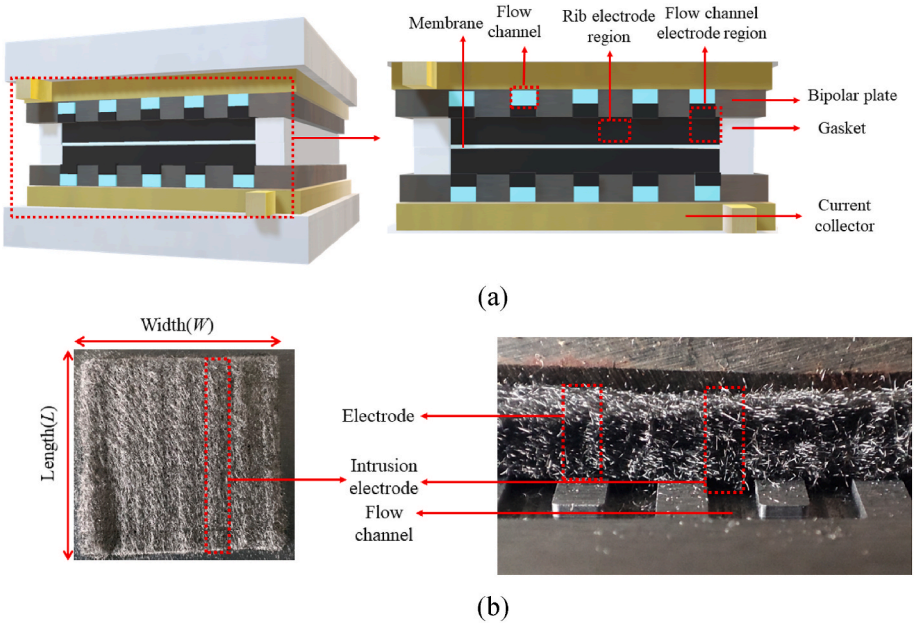

Fig. 1. An illustration of a VRB cell with unevenly compressed electrodes. (a) structure of a VRB cell, (b) electrodes present different regions due to uneven compression.

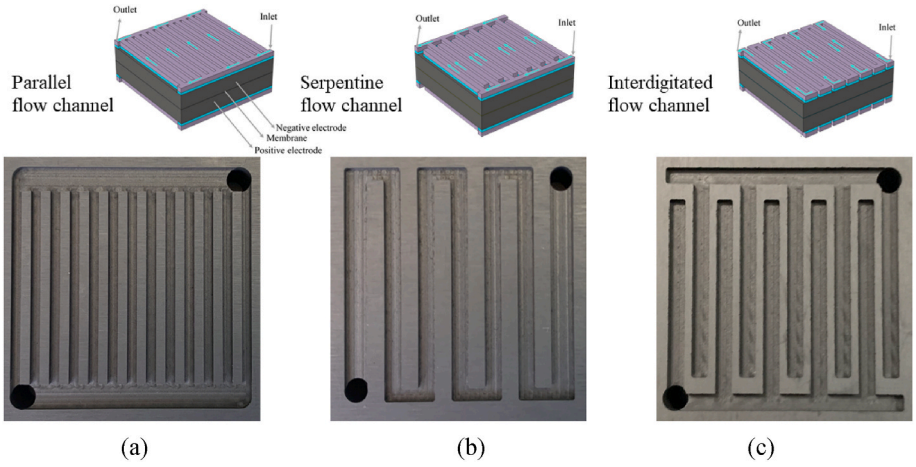

Fig. 2. Three designed flow fields: (a) parallel flow channel, (b) Serpentine flow channel, (c) Interdigitated flow channel.

$$\nabla \cdot \vec{i} = AFk_1(c_3)^{\alpha_{-,n}}(c_2)^{\alpha_{+,n}}\left[\exp\left(\frac{\alpha_{+,n}F\eta_1}{RT}\right) - \exp\left(\frac{\alpha_{-,n}F\eta_1}{RT}\right)\right] \tag{11}$$

$$\nabla \cdot \vec{i} = AFk_2(c_4)^{\alpha_{-,p}}(c_5)^{\alpha_{+,p}}\left[\exp\left(\frac{\alpha_{+,p}F\eta_2}{RT}\right) - \exp\left(\frac{\alpha_{-,p}F\eta_2}{RT}\right)\right] \tag{12}$$

where A is the specific surface area of the electrode, F is the Faraday constant with a value of 96485.33 C/mol, R is the gas constant with a value of 8.314 J/(mol·K), and T denotes the temperature. k_1 and k_2 are the standard rate constant of the negative and the positive electrode reaction, respectively. $\alpha_{+,n/p}$ and $\alpha_{-,n/p}$ are the transfer coefficients of the anode and cathode, respectively. $\alpha_{+,p}$ and $\alpha_{+,n}$ are approximated to 0.5. η_1 and η_2 are the overpotentials of the negative and positive electrodes, respectively, which are defined as:

$$\eta_1 = \varphi_s - \varphi_l - U_1 \tag{13}$$

$$\eta_2 = \varphi_s - \varphi_l - U_2 \tag{14}$$

where the open-circuit voltage U_1 and U_2 can be calculated by the Nernst equation:

$$U_1 = U_{10} + \frac{RT}{F}\ln\left(\frac{c_5}{c_4}\right) \tag{15}$$

$$U_2 = U_{20} + \frac{RT}{F}\ln\left(\frac{c_3}{c_2}\right) \tag{16}$$

where U_{10} and U_{20} are the standard equilibrium potentials, respectively.

Based on the charge conservation law, the net charge variation in a specific volume equals the charge flowing into the volume minus the charge flowing out of the volume. Since the vanadium electrolyte is electrically neutral, the charge conservation equation can be written as:

$$\nabla \vec{i_s} = -\nabla \vec{i_l} \tag{17}$$

$$\nabla \vec{i_s} = -\sigma_s^{eff}\nabla^2\varphi_s \tag{18}$$

$$-\nabla \vec{i_l} = \kappa_l^{\text{eff}}\nabla^2\varphi_l \tag{19}$$

where $\vec{i_s}$, $\vec{i_l}$, φ_s and φ_l represent the electron and ionic current densities, and the electron and ion potentials, respectively. σ_s^{eff} and κ_l^{eff} represent the effective electronic and ionic conductivities, respectively, given by

$$\sigma_s^{eff} = (1-\varepsilon)^{3/2}\sigma_s \tag{20}$$

$$\kappa_l^{\text{eff}} = \frac{F^2}{RT}\sum_i z_i^2 D_i^{eff} c_i \tag{21}$$

2.3. Boundary conditions

The boundary conditions such as the inlet flow rate and the outlet pressure drop are set to initialize the numerical analysis. The inlet flow rate of the cell is set to be Q_{in}, and the outlet pressure drop, P_{out}, is set to zero. For other boundaries, the second type of boundary conditions are applied, and the corresponding equations are shown as follows:

$$v = v_{in}\text{inlet}) \tag{22}$$

$$P = P_{out}\text{outlet}) \tag{23}$$

$$\nabla P \cdot \vec{n} = 0\text{ other boundaries}) \tag{24}$$

$$v_{in} = \frac{Q_{in}}{A_{in}} \tag{25}$$

where A_{in} denotes the cross-sectional area of the inlet flow channel and v_{in} is the inlet velocity.

The initial concentrations of vanadium ions are,

$$\begin{aligned} c_2^{in} &= c_n^0 \cdot SOC \\ c_3^{in} &= c_n^0 \cdot (1 - SOC) \\ c_4^{in} &= c_p^0 \cdot (1 - SOC) \\ c_5^{in} &= c_p^0 \cdot SOC \end{aligned} \tag{26}$$

where c_p^0 and c_n^0 are the total positive and negative vanadium ion concentrations, respectively. c_2^{in}, c_3^{in}, c_4^{in}, and c_5^{in} are the initial vanadium ion concentrations of 2, 3, 4, and 5. The fluxes of the other boundaries are set to zero.

$$-D_i^{eff}\nabla c_i \cdot \vec{n} = 0\text{ (outlet)} \tag{27}$$

$$\left(-D_i^{eff}\nabla c_i + c_i\vec{u}\right)\cdot\vec{n} = 0\text{ (the other boundaries)} \tag{28}$$

2.4. Numerical details

The electrochemical properties of the unevenly deformed model are listed in Table 1 below. The proposed model was implemented in the commercial software package COMSOL Multiphysics®, and solved by the finite element method. An average of 174,000 elements were applied to the simulation for all models.

Table 1
Electrochemical properties in the model.

Symbols	Parameter	Value	Origin
T	Temperature	297 (K)	
Q	Flow rate	30 (ml·min^{-1})	
i	Applied current density	40 (mA cm^{-2})	
ρ	Density of the electrolyte	1680 (kg m^{-3})	[21]
ε	Electrode porosity	0.9	[25]
A	Cell specific surface area	1.7×10^4 (m^{-1})	[30]
μ	Electrolyte dynamic viscosity	4.3×10^{-3} (Pa s)	[28]
U_{10} (VO^{2+}/ VO_2^+)	Equilibrium potential: 1.004 (V)	[31]	
U_{20} (V^{2+}/V^{3+})	Equilibrium potential: −0.255 (V)	[31]	
d_f	Electrode fiber diameter	11.94(μm)	
c^0	Half cell initial vanadium ion concentration	1500 (mol m^{-3})	
c_2^0	Initial V^{2+} ion concentration	1200 (mol m^{-3})	
c_3^0	Initial V^{3+} ion concentration	300 (mol m^{-3})	
c_4^0	Initial VO^{2+} ion concentration	1200 (mol m^{-3})	
c_5^0	Initial VO_2^+ ion concentration	300 (mol m^{-3})	
c_H^0	Initial H^+ ion concentration	6000 (mol m^{-3})	[32]
D_2, D_3	V^{2+}, V^{3+} diffusion coefficient	2.4×10^{-10} (m^2 s^{-1})	[33]
D_4D_5	VO^{2+},VO_2^+diffusion coefficient	3.9×10^{-10} (m^2 s^{-1})	[33]
D_H	H^+ diffusion coefficient	9.3×10^{-9} (m^2 s^{-1})	[34]
D_{SO4}	SO_4^{2+} diffusion coefficient	1.1×10^{-9} (m^2 s^{-1})	[34]
k_2	Standard reaction rate constant: positive	1.7×10^{-7} (m s^{-1})	[35]
k_1	Standard reaction rate constant: negative	6.8×10^{-7} (m s^{-1})	[36]
σ	Electronic conductivity	1×10^3 (S m^{-1})	[37]
$\alpha_{+,p}\alpha_{-,p}$	Anodic and Cathodic transfer coefficient: positive	0.5	[34]
$\alpha_{+,n}$, $\alpha_{-,n}$	Anodic and Cathodic transfer coefficient: negative	0.5	[34]

3. Experimental and simulation results

3.1. The electrode deformation testing under various CRs

To obtain the geometric details of the deformed electrodes, the electrode deformation testing by using various thickness of gaskets is carried out. The details of how to detect the morphological deformation of the electrodes are explained below. The electrode height directly affects the variation of porosity in the electrode. Here, porosity can be divided into electrode porosity and intrusion electrode porosity. The electrode deformation degree is adjusted by the thickness of the gaskets. Different thicknesses of FFPM gaskets (Manufacturer: Jing Tong Fuk Industrial Material Co. Ltd., China) are used to control the compression of the porous electrodes. A VRB compression testing sample is clamped by two aluminum plates with bolts, as shown in Fig. 3(a). The porous electrode firstly is placed within the aluminum plates and then the bolts are used to clamp them tightly. The surface area of two aluminum plates is 30 mm in width and 30 mm in length. The local porosity and intrusion thickness are analyzed by the scanning images obtained by cold field emission scanning electron microscope JEOL FJSM-7500F. The original thickness of carbon felt is 6 mm. In this paper, five sets of *CR*s, namely $CR = 1\%$,15%, 30%, 45%, and 60% are selected for investigation. And thus, five different thicknesses of gaskets (2.4 mm, 3.3 mm, 4.2 mm, 5.1 mm, and 6 mm) are used to clamp the electrode corresponding with electrode CRs of 60%, 45%, 30%, 15%, and 1%. The average fiber diameter is 11.94 μm.

The illustration of deformed electrode associated with electrode deformation, including the electrode thickness (h_e), intrusion electrode height (h_i), and flow channel height (h_f), is shown in Fig. 3(b). The porosity and the geometric parameters of the electrode are obtained and compared with experimental data in Ref. [25], and the corresponding parameters of the new *CR* are obtained by the curve fitting method. The relationship between *CR* and the porosity and geometric parameters are shown in Fig. 3 (c) and (d). The geometric parameters of electrode deformation of the VRB under different *CRs* are presented in Table 2.

An increase of mechanical stress will lead to a thinner layer with lower porosity. The deformation of the porous electrodes will affect the porosity, ε, and further affect the properties of the permeability, K, diffusivity, D and conductivity σ. Since the electrode is unevenly compressed by the rib patterns of the flow fields, the porosity under the rib region and the intrusion channel region are different. The parameters related to porosity: permeability, conductivity, and diffusivity are shown in Fig. 3(e–g). From Fig. 3(e), we can observe that the diffusion coefficient decreases as the porosity decreases. Similarly, from Fig. 3(f), as the porosity decreases, the permeability of the electrodes decreases and thus increases the pressure drop of the pumps. But the trend of electronic conductivity is reverse of porosity in Fig. 3(g), which indicates that the compressed carbon felt, to a certain extent, can reduce the electrode contact resistance.

3.2. The validation of the proposed unevenly deformed electrochemical model

To benchmark the proposed non-uniform electrochemical model with the real behavior of a single cell, the charge/discharge characteristic of a single cell is compared with the experimentally measured data by using the serpentine flow channel at CR = 15%. The experimental platform is shown in Fig. 4(a), including cell, pump, tank, high performance cell detection system and other components. To improve the accuracy of testing, three charge/discharge cycles are set to fully activate the cell activity to prevent performance loss of the cell due to some areas being activated. The charge/discharge experiment with a small constant current was carried out to reduce the impact of overpotential. The side reactions and polarization effects are ignored for simplification. The detailed specification of a single-cell vanadium redox flow battery is shown in Table 3.

The current density of 40 mA cm^{-2}, and the ambient temperature of 298.15 ± 1 K are applied for the experiment. The battery operations between 0.8 V and 1.7 V. Both in the simulation and experiment, the battery SOC is limited between 0.1 and 0.9. A comparison of the experimental and simulation curve are illustrated, and the maximum error of 112 mV and an average error of 2% is observed in Fig. 4(b). The results show that the numerical simulation results fit well with the experimental data in terms of charging/discharging voltage curves, which demonstrate the effectiveness of the proposed electrochemical model.

3.3. Analysis of the battery overpotentials

The cell overpotential is one of the key indicators to reflect the battery efficiency. To investigate how the *CRs* and the flow pattern affect the distribution of overpotential, a cross-section plane in the middle of the stack is selected, and the overpotential distribution is shown in Fig. 5, and the details of overpotential distribution under the parallel channel, serpentine channel, and interdigital channel are illustrated in Fig. 5 (a), (b) and (c), respectively. From Fig. 5(a), the overpotential under the parallel channel increases as the increase of electrolyte flow rates, reaching the maximum at the outlet. This phenomenon is due to the uneven distribution of electrolyte concentration. Since the concentration is depleted in the outlet, the concentration overpotential increases drastically. In contrast to the parallel channel, the overpotential fluctuations of the serpentine channel are much smooth and uniform at both inlet and outlet areas, as shown in Fig. 5(b). In Fig. 5(c), the overpotential of the interdigital channel has a similar trend to that of the serpentine channel. Due to the rapid depletion of vanadium concentration in the serpentine channel at the outlet area, the overpotential

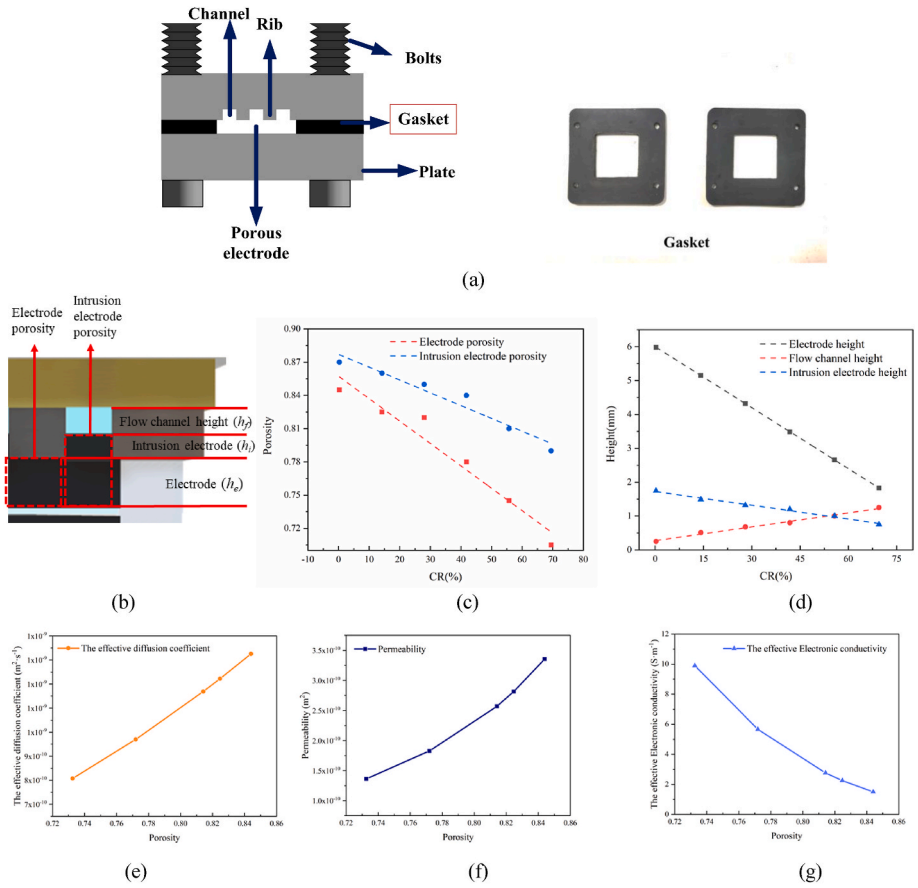

Fig. 3. The geometric details. (a) an illustration of the deformation testing by using various thickness of gaskets, (b) illustration of deformed electrode, (b) electrode porosity under different *CRs*, (d) geometric parameters of electrode deformation under different *CRs*, (e) the effective diffusion coefficient under various porosity, (f) the permeability coefficient under various porosities, (g) the conductivity coefficient under various porosities.

Table 2
Geometric parameters of electrode deformation of the VRB under different *CRs*.

Symbols	Parameter	Value				
		CR = 1%	CR = 15%	CR = 30%	CR = 45%	CR = 60%
L	Length of porous electrode	30 mm				
L_m	Membrane thickness	1 mm				
W	Width of porous electrode	30 mm				
W_{ch}	Channel width	1.5 mm				
h_f	Height of flow channel	1.74 mm	1.48 mm	1.30 mm	1.15 mm	0.92 mm
h_i	Intrusion region thickness	0.26 mm	0.52 mm	0.70 mm	0.85 mm	1.08 mm
h_e	Thickness of compressed electrode	5.94 mm	5.10 mm	4.20 mm	3.30 mm	2.40 mm

fluctuation at the outlet becomes larger. The average overpotentials of different *CRs* under three channels are illustrated in Fig. 5 (d). Although the overpotential fluctuation range of the serpentine channel is larger than the interdigitated channel at the outlet area, the serpentine channel has the minimum overpotential, whereas the parallel channel demonstrates the largest average overpotentials.

With the increase of *CRs*, the overpotentials of the three channels decrease initially and then begin to increase. The underlying fact is that the conductivity of electrodes and the permeability of the electrolyte vary and dominate each other under various *CRs*. From Fig. 5(d), the parallel channels reach the minimal overpotential under *CR* of 30%, whereas the serpentine and interdigitated channels reach the minimum value under *CR* of 45%, depending on whichever is dominant. As the *CRs* increase from 1% to 15%, a remarkable decrease in overpotential is observed. This is due to the decrease of porosities in the channel and rib electrodes, leading to an increase in the conductivity of the porous electrodes, according to (21). However, the decrease of porosities also indicates that the permeability of electrolytes is low, and the electrolytes are difficult to be penetrated into the flow channel. This will accelerate the concentration depletion in specific areas, especially around the corners of the cell, and thus an increase in overpotential.

3.4. Analysis of the pressure drop

The pressure drop is another indicator to reflect the batter performance, which describes the parasitic losses of the system under various flow rates. Since the pressure drop is significantly dependent on the electrolyte flow rate, the velocity distribution under various electrodes *CR* and flow channels are investigated. The electrolyte velocity distributions on a cross-section plane of the center of the stack are illustrated in Fig. 6. The velocity distributions at the inlet flow rate of 30 ml/min of the parallel, serpentine, and interdigital channels are shown in Fig. 6 (a), (b), and (c), respectively. The parallel channel demonstrates the lowest velocity, whereas the serpentine channel is the highest. In the parallel channel, multiple parallel branches are etched inside the stack, as shown in Fig. 2(a). The electrolytes are dispersed simultaneously, resulting in a rapid decline in the flow rates. However, the serpentine channel has only one main flow branch compared to the other channels, and the

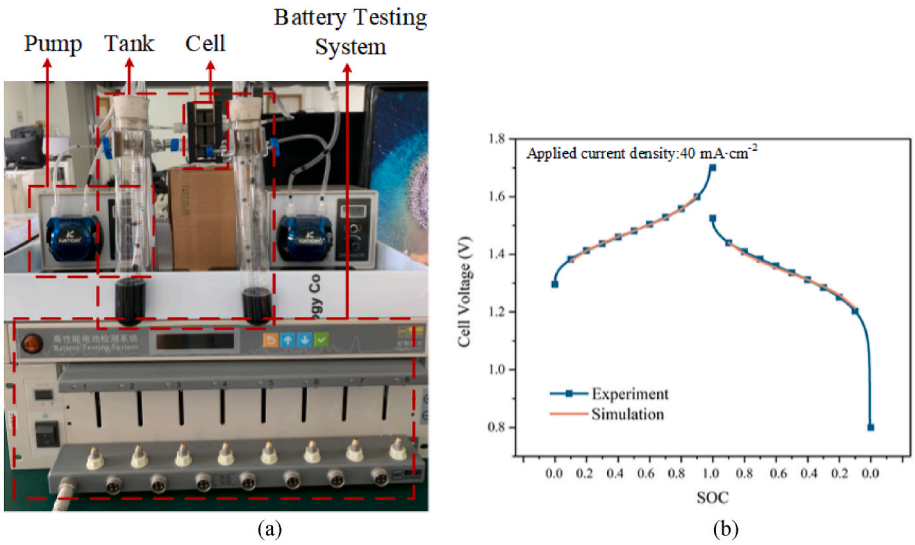

Fig. 4. Experimental validation: (a) Experiment platform, (b) Charge/discharge curves with serpentine flow field at CR = 15%.

Table 3
Specification of single cell VRB with serpentine flow field design at CR = 15%.

Configuration	Value
Flow channel	Serpentine flow channel
Active area	3 × 3 cm^2
Compression ratio	15%
Vanadium ion concentration	1500 mol m^{-3}
Flow rate	30 ml min^{-1}
Applied current density	40 mA cm^{-2}
Temperature	298.15 K
State of charge	0.1–0.9
Cell voltage limit	0.8–1.7 V
Electrolyte volume	25 ml

electrolyte cannot be dispersed to multiple branches, leading to the highest velocity. The trend observed from Fig. 6(a)–(b) is that as the *CR* increases, the electrolyte velocity of both the parallel and serpentine flow channels increases initially, reaching its maximum at CR of 30%, and then decreases. Compared with the other two channels, the interdigitated flow channel is not sensitive to the *CR* increase, according to Fig. 6(c). The electrolyte reaches a maximal velocity at *CR* of 60%. As the intrusion part of the electrodes compressed into the channel, the channel becomes larger, and a reduced cross-sectional area will accelerate the velocity of the electrolyte. As *CR* increases, a large compression rate of the electrodes may further lead to low porosity and thus hinder the electrolyte from penetrating the electrodes. An enlarged velocity distribution under *CR* of 60% is illustrated in Fig. 6(d). Among the three flow channel designs, the velocity of electrolyte in the parallel flow channel is obviously lower than in the other two.

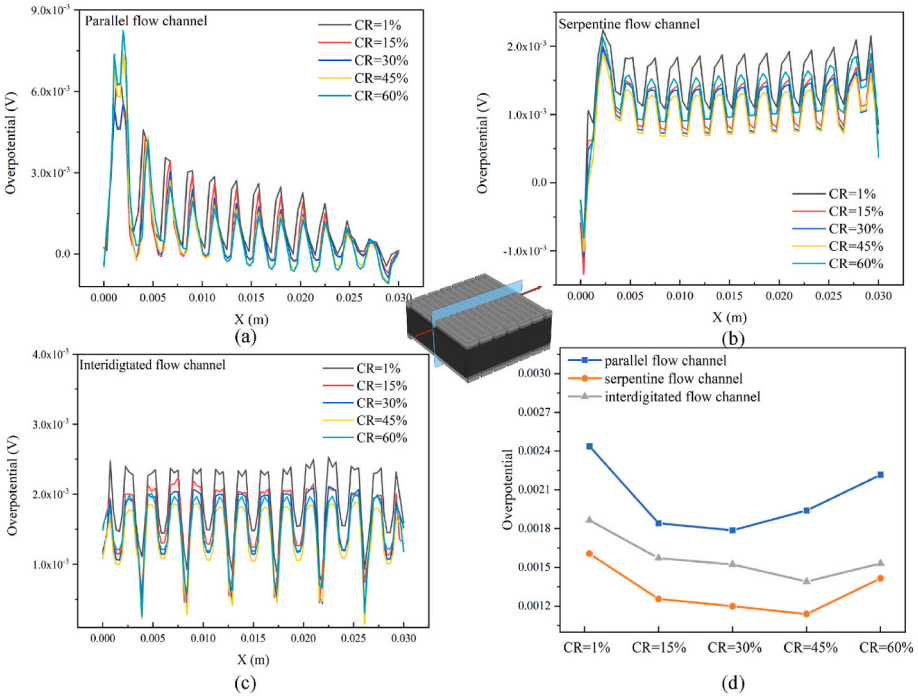

Fig. 5. Overpotential distribution under different electrode *CRs* and flow fields: (a) the overpotential of parallel flow channel, (b) the overpotential of serpentine flow channel, (c) the overpotential of interdigitated flow channel, (d) the average overpotential under three flow channels and *CRs*.

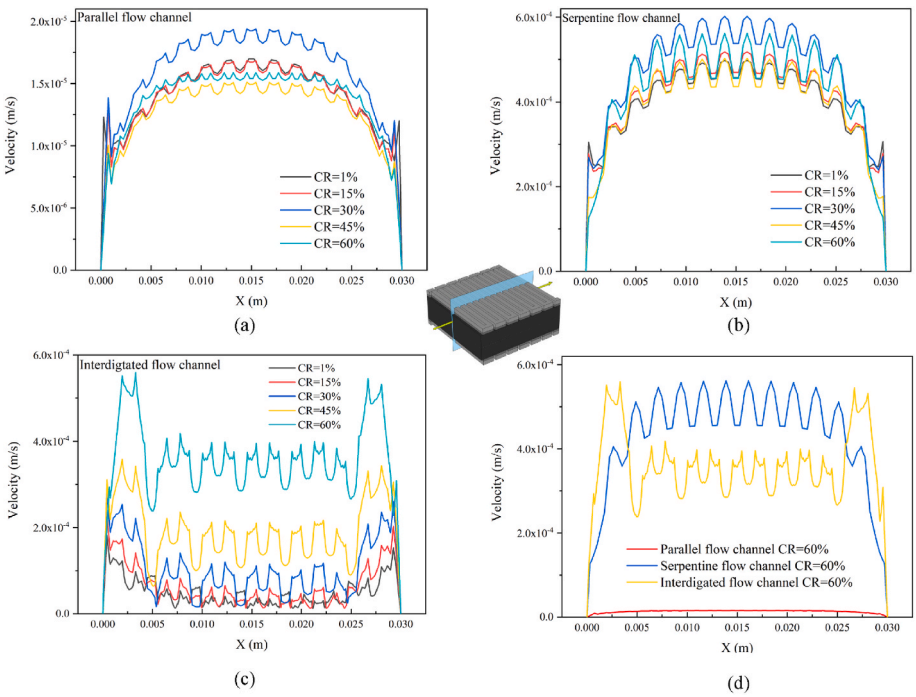

Fig. 6. Velocity distribution under different electrode CR and different flow fields: (a) the velocity of parallel flow channel, (b) the velocity of serpentine flow channel, (c) the velocity of interdigitated flow channel, (d) comparison of the three flow channels under $CR = 60\%$.

The pressure drop is highly related to the velocity of the electrolyte and reflects the parasitic loss of system. A high pressure drop will lead to low battery efficiency. The pressure drop of three flow channels under various flow rates is shown in Fig. 7(a)-(c), respectively. Among these flow channels, the parallel flow channel demonstrates the lowest pressure drop, while the serpentine flow channel demonstrate the highest pressure drop. The pressure drop is highly sensitive to the both of flow rates and *CR*s. The pressure drop under various CRs is further plotted in Fig. 7(d). From this figure, the slope of the pressure drop shifts significant after *CR* reaches to 45%. When the *CR* value is beyond 60%, the pressure drop increases rapidly. Therefore, the candidate value of *CR* can be selected below 45%. The parallel flow channel exhibits a low pressure drop since the electrolyte flows into the multiple branches and thus results in a low velocity. But the serpentine channel has a single

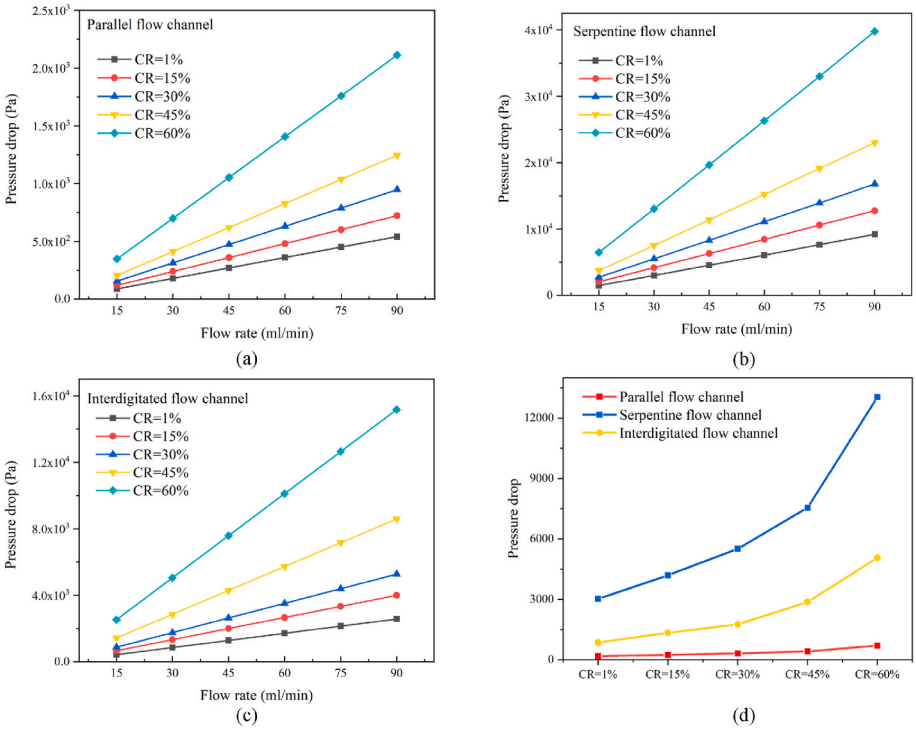

Fig. 7. The pressure drop of three flow channels under various flow rates and electrodes *CR*s: (a) the pressure drop of parallel flow channel, (b) the pressure drop of serpentine flow channel, (c) the pressure drop of interdigitated flow channel, (d) the pressure drop under various *CR*s.

long branch throughout the stack, which significantly increases the pressure drop.

3.5. Analysis of the concentration distribution

The concentration distribution is another key indicator for analyzing the cell performance, which describes the heterogeneity of the electrolyte concentration. The unevenly distributed concentration may lead to severe problems such as local hot spots and high concentration overpotential. To describe the electrolyte concentration distribution, a quantitative metric named the uniformity coefficient, C, is defined as,

$$C = 1 - \frac{1}{C_{ia}}\sqrt{\frac{1}{V+V_i}\iiint_{V+V_i}(C_i - C_{\mathrm{ia}})^2 d(V+V_i)} \tag{29}$$

where V is the volume of the porous electrode, V_i is the volume of the intrusion electrode. C_i is the local concentration of active species in the porous electrodes, and C_{ia} is the average concentration of active species in the electrodes.

To illustrate the electrolyte concentration distribution, the cross-section view of the concentration distribution of V^{2+} and VO_2^+ is shown in Fig. 8. From Fig. 8(a1-a3), the parallel flow channel exhibits a highly uneven concentration distribution. And a concentration depletion near the outlet of the parallel flow channel is observed compared with the other two flow channels. The depletion of local concentration can lead to a high overpotential, causing overheating and damaging the cell. From Fig. 8(b1-b3), a more uniform concentration distribution is exhibited in the serpentine flow channel since a higher velocity of electrolyte would replenish active species in time. The detailed concentration distribution of the interdigitated flow channel is illustrated in Fig. 8(c1-c3). Different from the other two channels, where the concentration difference has a distinguished distribution from left to right, the concentration difference for the interdigitated flow channel has a distinguished distribution from upper to lower, reducing the risk of overheating due to the local spot concentration depletion.

The concentration uniformity of the V^{2+} ion concentration at different *CR*s and flow channels is shown in Fig. 9(a). The parallel flow channel in red curve demonstrates a low uniformity concentration and is very sensitive to the variations of *CR*s compared with the other two channels. The concentration uniformity coefficient of the parallel flow channel increases initially, reaching a maximum of 0.891 under a *CR* of 15%, and then decreases rapidly under a higher *CR*. Since the internal velocity of such a channel is relatively slow, the concentration becomes unevenly distributed under such low velocity. In contrast to the parallel flow channel, the serpentine and interdigitated flow channel demonstrate a high concentration uniformity with an average value of 0.983, and they are not sensitive to the variation of *CR*s.

The spider chart of the performance analysis under three different flow channels and *CR*s are shown in Fig. 9(b–c). From Fig. 9 (b), the parallel flow channel demonstrates excellent performance in terms of the pressure drop but a high overpotential and a low concentration uniformity distribution. And the concentration uniformity of the parallel flow channel is sensitive to the electrode deformation and reaches its maximum under CR of 15%. From Fig. 9(c), the serpentine flow channel outperformed in terms of the overpotential and concentration uniformity distribution but consumed a high pressure drop. The minimum overpotential can be reached when the CR is around 40%–50%. From Fig. 9(d), the interdigitated flow channel maintains a low overpotential and a high concentration uniformity distribution under CRs from 30% to 45%. To consider the overall performance, the interdigitated flow

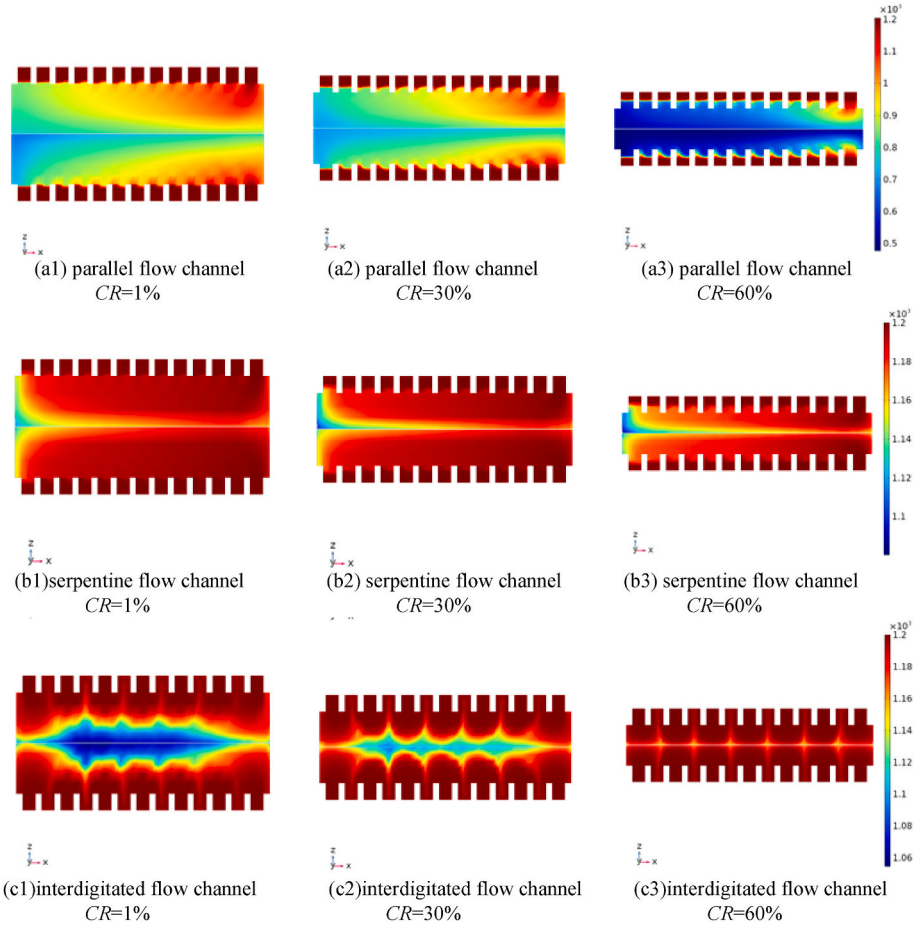

Fig. 8. The concentration distribution of V^{2+} and VO_2^+ for various electrode compression and flow channels.

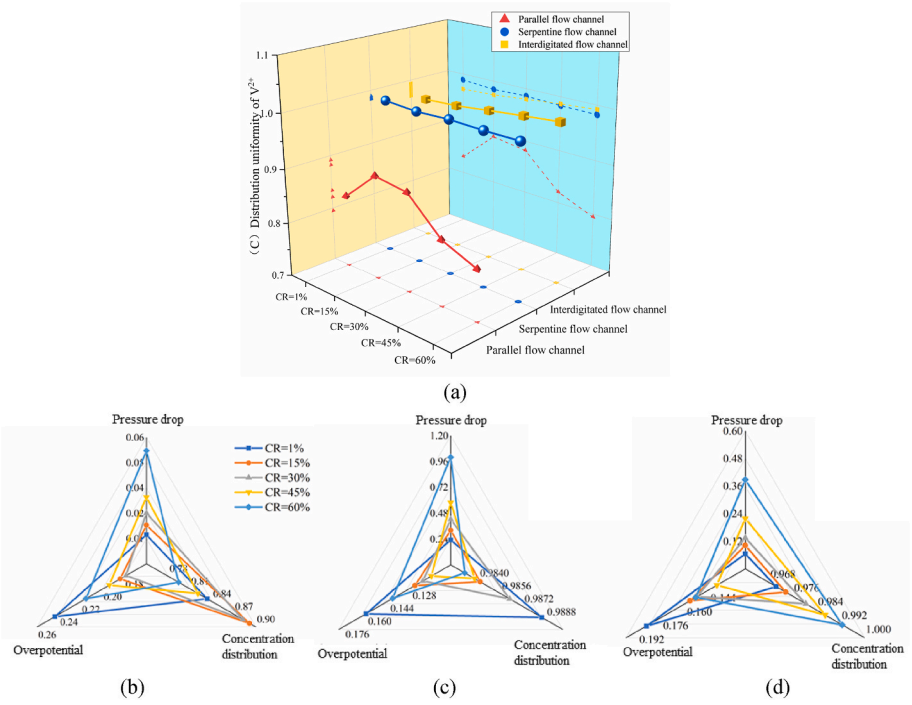

Fig. 9. The performance analysis under different flow channels and *CRs*: (a) the concentration uniformity of V^{2+} ion concentration at different *CRs* and flow channels. (b) the spider chart of the performance of parallel flow channel, (c) the spider chart of the performance of the serpentine flow channel, (d) the spider chart of the performance of the interdigitated flow channel.

channel with CR = 45% is recommended to balance the concentration uniformity, the overpotential, and the pressure drop.

4. Conclusion

In this paper, an unevenly deformed electrochemical model is established to investigate the overall VRB performance under different compression ratios and different flow channels. Three indices, namely the concentration overpotential, pressure drop, and distribution uniformity, are selected for the analysis under the three flow field designs. The numerical study reveals that the pressure drop and the concentration overpotential are sensitive to the CR but less affected by the concentration uniformity. The interdigitated flow field with a CR of 45% is recommended considering the effects of electrode deformation in the stack design under various flow fields.

CRediT authorship contribution statement

Binyu Xiong: Methodology, Writing – original draft, Writing – review & editing. **Yang Li:** Visualization, Validation, Writing – review & editing. **Jinsong Wang:** Writing – review & editing. **Zhongbao Wei:** Investigation, Formal analysis. **Jiyun Zhao:** Investigation. **Jiakun Fang:** Conceptualization, Methodology, Supervision.

Declaration of competing interest

The authors declare the following financial interests/personal relationships which may be considered as potential competing interests: BINYU XIONG reports financial support was provided by National Natural Science Foundation of China.

Data availability

No data was used for the research described in the article.

Acknowledgment

This work was supported by the National Natural Science Foundation of China under Grant No.52177221.

References

[1] K. Lourenssen, J. Williams, F. Ahmadpour, R. Clemmer, S. Tasnim, Vanadium redox flow batteries: a comprehensive review, J. Energy Storage 25 (2019), 100844, https://doi.org/10.1016/j.est.2019.100844.
[2] B. Xiong, Y. Yang, J. Tang, Y. Li, Z. Wei, Y. Su, Q. Zhang, An enhanced equivalent circuit model of vanadium redox flow battery energy storage systems considering thermal effects, IEEE Access 7 (2019) 162297–162308, https://doi.org/10.1109/ACCESS.2019.2952212.
[3] C. Minke, T. Turek, Materials, system designs and modelling approaches in techno-economic assessment of all-vanadium redox flow batteries – a review, J. Power Sources 376 (2018) 66–81, https://doi.org/10.1016/j.jpowsour.2017.11.058.
[4] W. Lu, Z. Yuan, Y. Zhao, H. Zhang, H. Zhang, X. Li, Porous membranes in secondary battery technologies, Chem. Soc. Rev. 46 (2017) 2199–2236, https://doi.org/10.1039/C6CS00823B.
[5] Y. Leng, P. Ming, D. Yang, C. Zhang, Steel bipolar plates for proton exchange membrane fuel cells: materials, flow channel design and forming processes, J. Power Sources 451 (2020), 227783, https://doi.org/10.1016/j.jpowsour.2020.227783.
[6] Y. Zhang, L. Liu, J. Xi, Z. Wu, X. Qiu, The benefits and limitations of electrolyte mixing in vanadium flow batteries, Appl. Energy 204 (2017) 373–381, https://doi.org/10.1016/j.apenergy.2017.07.049.
[7] J. Xiong, Y. Song, S. Wang, X. Li, J. Liu, C. Yan, A. Tang, Evaluation of the influence of clamping force in electrochemical performance and reliability of vanadium redox flow battery, J. Power Sources 431 (2019) 170–181, https://doi.org/10.1016/j.jpowsour.2019.05.061.
[8] T. Jirabovornwisut, S. Kheawhom, Y.-S. Chen, A. Arpornwichanop, Optimal operational strategy for a vanadium redox flow battery, Comput. Chem. Eng. 136 (2020), 106805, https://doi.org/10.1016/j.compchemeng.2020.106805.
[9] B. Xiong, J. Zhao, Y. Su, Z. Wei, M. Skyllas-Kazacos, State of charge estimation of vanadium redox flow battery based on sliding mode observer and dynamic model including capacity fading factor, IEEE Trans. Sustain. Energy 8 (2017) 1658–1667, https://doi.org/10.1109/TSTE.2017.2699288.
[10] C. Zhang, L. Zhang, Y. Ding, S. Peng, X. Guo, Y. Zhao, G. He, G. Yu, Progress and prospects of next-generation redox flow batteries, Energy Storage Mater. 15 (2018) 324–350, https://doi.org/10.1016/j.ensm.2018.06.008.
[11] M. Wu, M. Liu, G. Long, K. Wan, Z. Liang, T.S. Zhao, A novel high-energy-density positive electrolyte with multiple redox couples for redox flow batteries, Appl. Energy 136 (2014) 576–581, https://doi.org/10.1016/j.apenergy.2014.09.076.

[12] H. Ishitobi, J. Saito, S. Sugawara, K. Oba, N. Nakagawa, Visualized cell characteristics by a two-dimensional model of vanadium redox flow battery with interdigitated channel and thin active electrode, Electrochim. Acta 313 (2019) 513–522, https://doi.org/10.1016/j.electacta.2019.04.055.
[13] E. Ali, H. Kwon, J. Kim, H. Park, Numerical study on serpentine design flow channel configurations for vanadium redox flow batteries, J. Energy Storage 32 (2020), 101802, https://doi.org/10.1016/j.est.2020.101802.
[14] Z. Huang, A. Mu, L. Wu, H. Wang, Vanadium redox flow batteries: flow field design and flow rate optimization, J. Energy Storage (2021), 103526, https://doi.org/10.1016/j.est.2021.103526.
[15] J.Q. Chen, B.G. Wang, H.L. Lv, Numerical simulation and experiment on the electrolyte flow distribution for all vanadium redox flow battery, Adv. Mater. Res. 236–238 (2011) 604–607. https://doi.org/10.4028/www.scientific.net/AMR.236-238.604.
[16] Y.-H. Jiao, M.-Y. Lu, W.-W. Yang, X.-Y. Tang, M. Ye, Q. Xu, A 3D macro-segment network model for vanadium redox flow battery with serpentine flow field, Electrochim. Acta 403 (2022), 139657, https://doi.org/10.1016/j.electacta.2021.139657.
[17] M.-Y. Lu, Y.-M. Deng, W.-W. Yang, M. Ye, Y.-H. Jiao, Q. Xu, A novel rotary serpentine flow field with improved electrolyte penetration and species distribution for vanadium redox flow battery, Electrochim. Acta 361 (2020), 137089, https://doi.org/10.1016/j.electacta.2020.137089.
[18] M. Messaggi, P. Canzi, R. Mereu, A. Baricci, F. Inzoli, A. Casalegno, M. Zago, Analysis of flow field design on vanadium redox flow battery performance: development of 3D computational fluid dynamic model and experimental validation, Appl. Energy 228 (2018) 1057–1070, https://doi.org/10.1016/j.apenergy.2018.06.148.
[19] J. Houser, A. Pezeshki, J.T. Clement, D. Aaron, M.M. Mench, Architecture for improved mass transport and system performance in redox flow batteries, J. Power Sources 351 (2017) 96–105, https://doi.org/10.1016/j.jpowsour.2017.03.083.
[20] S.-K. Park, J. Shim, J.H. Yang, C.-S. Jin, B.S. Lee, Y.-S. Lee, K.-H. Shin, J.-D. Jeon, The influence of compressed carbon felt electrodes on the performance of a vanadium redox flow battery, Electrochim. Acta 116 (2014) 447–452, https://doi.org/10.1016/j.electacta.2013.11.073.
[21] D. You, H. Zhang, J. Chen, A simple model for the vanadium redox battery, Electrochim. Acta 54 (2009) 6827–6836, https://doi.org/10.1016/j.electacta.2009.06.086.
[22] K. Bromberger, J. Kaunert, T. Smolinka, A model for all-vanadium redox flow batteries: introducing electrode-compression effects on voltage losses and hydraulics, Energy Technol. 2 (2014) 64–76, https://doi.org/10.1002/ente.201300114.
[23] K. Oh, S. Won, H. Ju, Numerical study of the effects of carbon felt electrode compression in all-vanadium redox flow batteries, Electrochim. Acta 181 (2015) 13–23, https://doi.org/10.1016/j.electacta.2015.02.212.
[24] L.D. Brown, T.P. Neville, R. Jervis, T.J. Mason, P.R. Shearing, D.J.L. Brett, The effect of felt compression on the performance and pressure drop of all-vanadium redox flow batteries, J. Energy Storage 8 (2016) 91–98, https://doi.org/10.1016/j.est.2016.10.003.
[25] Q. Wang, Z.G. Qu, Z.Y. Jiang, W.W. Yang, Numerical study on vanadium redox flow battery performance with non-uniformly compressed electrode and serpentine flow field, Appl. Energy 220 (2018) 106–116, https://doi.org/10.1016/j.apenergy.2018.03.058.
[26] R. Xiong, B. Xiong, Q. Zhang, S. Shi, Y. Su, D. Zhang, Capacity fading model of vanadium redox flow battery considering water molecules migration, Int. J. Green Energy (2022) 1–10, https://doi.org/10.1080/15435075.2021.2015599.
[27] M. Yue, Q. Zheng, F. Xing, H. Zhang, X. Li, X. Ma, Flow field design and optimization of high power density vanadium flow batteries: a novel trapezoid flow battery, AIChE J. 64 (2018) 782–795, https://doi.org/10.1002/aic.15959.
[28] Q. Zheng, H. Zhang, F. Xing, X. Ma, X. Li, G. Ning, A three-dimensional model for thermal analysis in a vanadium flow battery, Appl. Energy 113 (2014) 1675–1685, https://doi.org/10.1016/j.apenergy.2013.09.021.
[29] Q. Xu, T.S. Zhao, Fundamental models for flow batteries, Prog. Energy Combust. Sci. 49 (2015) 40–58, https://doi.org/10.1016/j.pecs.2015.02.001.
[30] Y.K. Zeng, T.S. Zhao, L. An, X.L. Zhou, L. Wei, A comparative study of all-vanadium and iron-chromium redox flow batteries for large-scale energy storage, J. Power Sources 300 (2015) 438–443, https://doi.org/10.1016/j.jpowsour.2015.09.100.
[31] M. Vynnycky, Analysis of a model for the operation of a vanadium redox battery, Energy 36 (2011) 2242–2256, https://doi.org/10.1016/j.energy.2010.03.060.
[32] A.A. Shah, M.J. Watt-Smith, F.C. Walsh, A dynamic performance model for redox-flow batteries involving soluble species, Electrochim. Acta 53 (2008) 8087–8100, https://doi.org/10.1016/j.electacta.2008.05.067.
[33] K.W. Knehr, E. Agar, C.R. Dennison, A.R. Kalidindi, E.C. Kumbur, A transient vanadium flow battery model incorporating vanadium crossover and water transport through the membrane, J. Electrochem. Soc. 159 (2012) A1446–A1459, https://doi.org/10.1149/2.017209jes.
[34] Y. Lei, B.W. Zhang, B.F. Bai, T.S. Zhao, A transient electrochemical model incorporating the Donnan effect for all-vanadium redox flow batteries, J. Power Sources 299 (2015) 202–211, https://doi.org/10.1016/j.jpowsour.2015.08.100.
[35] X. Ma, H. Zhang, F. Xing, A three-dimensional model for negative half cell of the vanadium redox flow battery, Electrochim. Acta 58 (2011) 238–246, https://doi.org/10.1016/j.electacta.2011.09.042.
[36] F. Li, Y. Wei, P. Tan, Y. Zeng, Y. Yuan, Numerical investigations of effects of the interdigitated channel spacing on overall performance of vanadium redox flow batteries, J. Energy Storage 32 (2020), 101781, https://doi.org/10.1016/j.est.2020.101781.
[37] J. Lee, J. Kim, H. Park, Numerical simulation of the power-based efficiency in vanadium redox flow battery with different serpentine channel size, Int. J. Hydrogen Energy 44 (2019) 29483–29492, https://doi.org/10.1016/j.ijhydene.2019.05.013.